metals

MDPI

Article

Influence of Heat Input on the Formation of Laves Phases and Hot Cracking in Plasma Arc Welding (PAW) Additive Manufacturing of Inconel 718

Teresa Artaza [1], Trunal Bhujangrao [1], Alfredo Suárez [1], Fernando Veiga [1,*] and Aitzol Lamikiz [2]

[1] TECNALIA, Basque Research and Technology Alliance (BRTA), Parque Científico y Tecnológico de Gipuzkoa, E20009 Donostia-San Sebastián, Spain; teresa.artaza@tecnalia.com (T.A.); trunal.bhujangrao@tecnalia.com (T.B.); alfredo.suarez@tecnalia.com (A.S.);

[2] Department of Mechanical Engineering, University of the Basque Country (UPV/EHU), E48013 Bilbao, Spain; aitzol.lamikiz@ehu.eus

* Correspondence:fernando.veiga@tecnalia.com; Tel.: +34-902-760-000

Received: 20 May 2020; Accepted: 8 June 2020; Published: 9 June 2020

Abstract: Nickel-based alloys have had extensive immersion in the manufacturing world in recent decades, especially in high added value sectors such as the aeronautical sector. Inconel 718 is the most widespread in terms of implantation. Therefore, the interest in adapting the manufacture of this material to additive manufacturing technologies is a significant objective within the scientific community. Among these technologies for the manufacture of parts by material deposition, plasma arc welding (PAW) has advantages derived from its simplicity for automation and integration on the work floor with high deposition ratios. These characteristics make it very economically appetizing. However, given the tendency of this material to form precipitates in its microstructure, its manufacturing by additive methods is very challenging. In this article, three deposition conditions are analyzed in which the energy and deposition ratio used are varied, and two cooling strategies are studied. The interpass cooling strategy (ICS) in which a fixed time is expected between passes and controlled overlay strategy (COS) in which the temperature at which the next welding pass starts is controlled. This COS strategy turns out to be advantageous from the point of view of the manufacturing time, but the deposition conditions must be correctly defined to avoid the formation of Laves phases and hot cracking in the final workpiece.

Keywords: additive manufacturing; WAAM; PAW; nickel-based alloys; hot cracking; microstructure

1. Introduction

Nickel-based IN718 superalloy is widely used in many industries like aerospace, automobile, shipbuilding and energy for manufacturing complex parts. IN718 alloy has very high strength at high temperatures, high fatigue, creep-rupture strength, excellent oxidation resistance properties and high resistance to postweld cracking which allows using the components from this material in any aggressive environment [1–3].

Manufacturing parts from these superalloys (IN718) using conventional processes is a challenging task and expensive. Hence, it requires cost-effective manufacturing methods that reduce material wastage, enhance design freedom and shorten production time. Additive manufacturing offers these benefits producing a vast range of shapes and designs. It has a huge economic advantage as well as being environmentally friendly [4].

Additive manufacturing (AM) is a group of nonconventional manufacturing processes that produce components by adding material in a layer-by-layer fashion, which is able to obtain the final shape of the component in accordance with the CAD model [5]. Additive manufacturing is capable

of producing complex designs and three-dimensional structures that are impossible or considerably expensive for conventional processes like turning, milling, grinding, drilling, etc. Hence, the AM process leads to developments in the production of geometrically large metallic components like turbines, engines as well as advancements in the biomedical industry [6].

Arc-based AM processes like wire + arc additive manufacturing (WAAM) [7] are adequate for manufacturing large-sized parts and characterized by a high deposition rate and low equipment costs [8]. WAAM uses an electric arc as a heat source to simultaneously melt and deposit metal wire as a feedstock onto a substrate, as a result of building up a part layer-by-layer. Fundamental suitable property of the WAAM is weldability. IN718 is one of the most weldable superalloys.

The deposition of IN718 in WAAM techniques has been studied by using an inert metal gas (MIG) [9], tungsten inert gas (TIG) [10], cold metal transfer (CMT) [11] and plasma arc welding (PAW) [12]. Plasma arc welding (PAW) is a high energy density process; the deposition rate and temperature during PAW are very high. Therefore, the cooling rates of each layer in the WAAM material differ locally. As a result of that, some solidification defects, such as solute segregation and undesirable Laves phase in the interdendritic regions, randomly form during solidification.

The alloy is vulnerable to severe segregation during solidification. Nb is one of the essential elements for the formation of the NbC and Laves phase [13]. Ye et al. [14] reported that the solidification cracking of IN718 is closely related to the carbides and Laves eutectic constituents that formed along the grain boundaries. The segregation and Laves phase increase the embrittling effect of the material, which leads to the formation of hot cracking in several locations and in different orientations of the WAAM IN718. The formation of these Laves phase is deleterious the microstructure and mechanical properties.

There are several ways to deal with the formation of the Laves phase and hot cracking. Deng et al. [15] determined that a slight variation in the Nb, Ni and Ti composition of IN718 feed wire, decreases the formation of the Laves phase and improves the mechanical properties of the WAAM IN718. Xu et al. [16] reported that the postdeposition homogenization heat treatment not only dissolves the Laves phase back into the matrix but improves the microstructure and elastic properties. Yangfan et al. [17] used the different heat input to increase the welding cooling time in the TIG process to reduce the hot cracking. The casting process of In718 [18] shows that the Laves phase significantly decreases by increasing the cooling rate. For example, no Laves phase was found in the alloys solidified at a very high cooling rate in the levitation experiment [19]. Therefore, the cooling rate is one of the most important technological parameters that should be controlled during manufacturing complex WAAM IN718 parts. This improves the microstructure and mechanical properties [20] and achieves a maximum instantaneous cooling rate using the pulse current mode in the TIG process, reducing interdendritic microsegregation and the Laves phase.

In this paper, the WAAM IN718 wall is manufactured by using plasma arc welding with different heat input strategies in terms of current and voltage parameters and interlayer time strategies. The interpass cooling strategy is used in order to monitor the solidification rate of each deposition layer to estimate the effect of interpass cooling in the microstructure and mechanical properties of IN718 alloy. Processing parameters like torch travel speed, wire feed rate, interpass time and temperature between the deposition layers are controlled by the EWM welding system. The effect of cooling rate on solidification cracking, Laves phase, segregation and the heat-affected zone was studied. Microstructure analysis, the microhardness of the WAAM material, composition of elements and initiation of hot cracking are investigated.

2. Materials and Methods

2.1. Experimental Set-Up

A five-axis gantry machine was used to manufacture the WAAM IN718 wall, as shown in Figure 1. The machine is powered by a Tetrix 552 AC/DC Synergic Plasma EWM AG (Mündersbach, Germany) arc welding system that provides up to 420 A; it generates the direct flow of the plasm

through plasma torch. A special protective closure chamber is used for manufacturing reactive material like IN718, Titanium, etc.

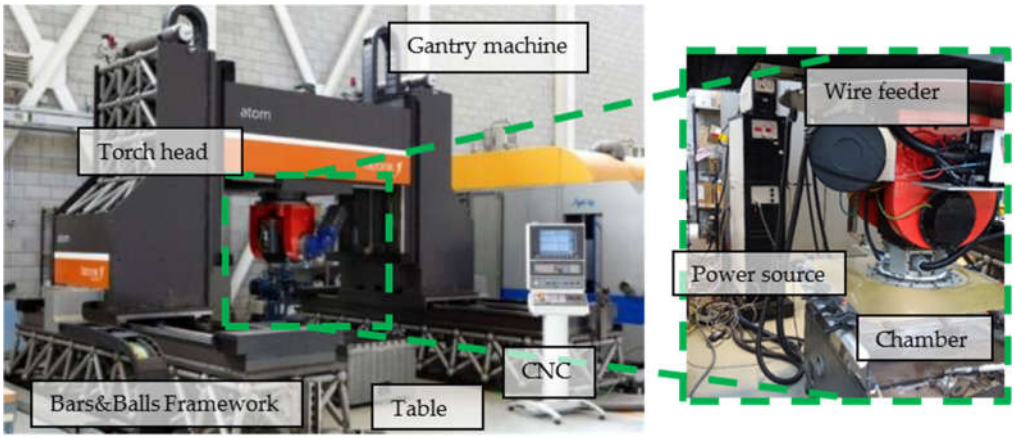

Figure 1. Shaft gantry machine with EWM welding equipment.

In addition, the ATOM machine from Tecnalia (San Sebastian, Spain) incorporates several sensors (Figure 2): an oxygen sensor, a laser profilometer, a pyrometer and a welding camera. The set of these sensors allows controlling the process to the maximum, together with the internal signals acquired from the welding equipment itself. The signals of the sensors are synchronized with the machine positions, which allows obtaining information on each point where the material was deposited. A computer was used for running the master application for monitoring the process.

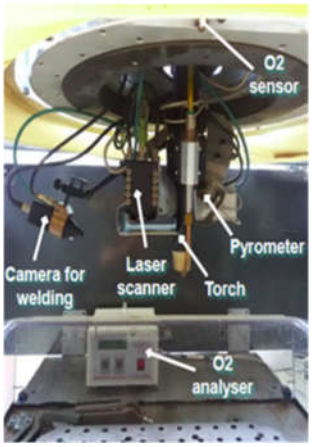

Figure 2. Sensors installed in the machine head.

2.2. Deposition Strategy and Parameters

An experiment was carried out on a substrate (base material with a thickness of 10 mm) fixed to the welding table. Manufacturing parameters corresponding to the wall were loaded in a library of the special software designed for this process. This software was used to program the tool paths and the initial and final points of the welder and a wire feeder. Finally, the welding was begun by depositing the number of layers in a normal layer-by-layer fashion.

The wire used for this study was 1.2 mm of IN718. The chemical composition is listed in Table 1. The wire feed rate remains constant for all the layers. Argon gas was used as a plasma gas and shielding gas, a flow rate of 12 L/min was used to protect the material from the outside environment, whereas the oxygen level was controlled below 100 ppm. The plasma gas flow rate was 1.5 L/min.

Table 1. Chemical composition of IN718 wire (wt %).

Ni	Cr	Nb + Ta	Mo	Ti	Al	Co	Mn	Fe
52.3	18.81	5.33	3.2	0.96	0.53	0.35	0.15	Bal.

It is a well-established fact that among all the welding parameters in plasma arc welding processes, the welding current is the most controlling variable since it affects the melting rate of the wire as well as the base material. So, in accordance with this fundamental fact, the two different continuous current inputs selected for the present study with the combination of different processing parameters (A, B and C) required for high production of the IN718 were listed in Table 2. There is a reason for using these specific welding current values, this range of processing parameter input combinations results in arc energies which were sufficient to cause adequate fusion of the base and wire selected for the present study.

Table 2. Process parameters for the manufacture of IN718 WAAM wall.

Test ID	Interpass Cooling Strategy (ICS)	Test ID	Continuous Overlayer Strategy (COS)	TTS: Torch Travel Speed (mm/min)	WFS: Wire Feed Speed (m/min)	DR: Deposition Rate (kg/h)
A_ICS	180 s	A_COS	500 °C	402	6.0	3.33
B_ICS	180 s	B_COS	500 °C	230	2.5	1.39
C_ICS	180 s	C_COS	500 °C	230	1.5	0.83

The interpass cooling temperature was also considered as a variable to control the thermal deposition in the WAAM process. Two different strategies were used in this study to fabricate the wall by using both the interpass cooling strategy (ICS) and controlled overlayer strategy (COS) for each combination of the processing parameters. The wall was manufactured by depositing single and superimposing layers on top of the flat substrate until the final wall with 12 layers. The alternating layers were deposited in opposite directions in order not to lose geometric tolerance. The graphical representation is shown in Figure 3. The interpass cooling temperature for ICS was set at 300 °C of the wall surface; it was monitored and controlled by a pyrometer to maintain the same temperature for each layer. Thus, this appropriate interpass cooling temperature was chosen to maintain the quality of the parts without incurring excessive time penalties.

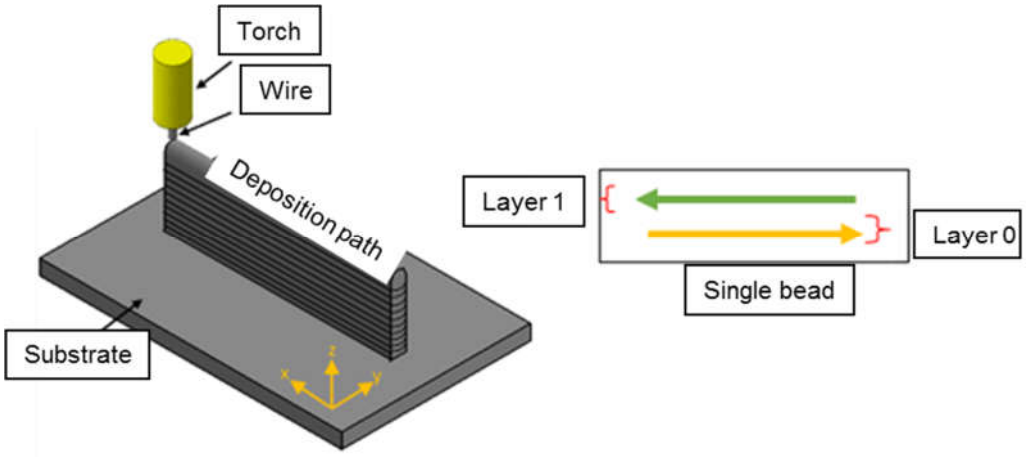

Figure 3. Graphical representation of the layer sequence.

Finally, to monitor the geometric shape of each layer, the laser scanner was used placed next to the plasma torch. This laser scanner continuously acquires three-dimensional information of the layer; it was possible to calculate how much the wall has grown easily. In addition to that, all welding

data was monitored and saved for further processing. Figure 4 shows the WAAM walls fabricated by using the three different processing parameters (A, B and C) with the two different deposition strategies, ICS and COS. No visible hot cracking or any defects were observed on the inner surface.

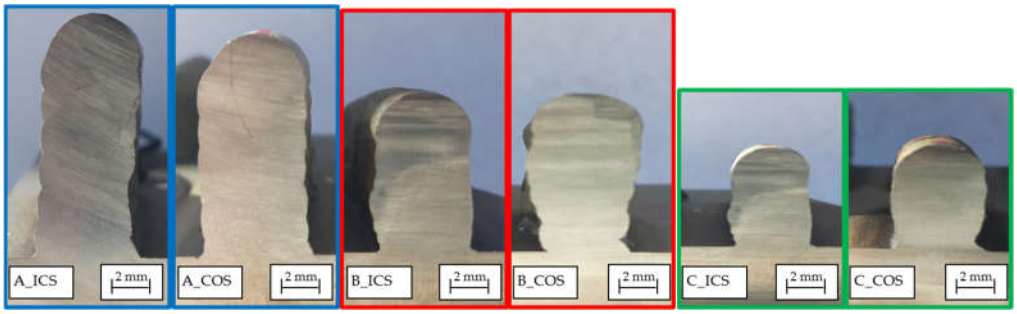

Figure 4. Traverse view of deposited wire + arc additive manufacturing (WAAM) wall by using three different processing parameters (A, B and C) with two different cooling strategies (interpass cooling strategy (ICS) and controlled overlay strategy (COS)).

In order to observe the microstructural changes that took place during plasma arc welding, corresponding to each processing parameter with respect to ICS and COS, the specimens were cut from the center area and the cross-section of the WAAM wall was observed. Standard polishing procedures were used for general microstructural observations (40 mL of hydrochloric acid and 3 mL of H_2O_2). Microstructures of the interested zone like weld metal, heat-affected zone (HAZ) and fusion boundary under different wall structures were viewed and captured with an optical microscope. The microstructures were characterized using scanning electron microscopy (JEOL (Tokio, Japan) JSM-5910LV microscope with an Oxford EDX INCA X-act), and composition of the element was measured using energy-dispersive spectrometry (EDS).

3. Results and Discussion

3.1. Process Characterization

In this section, considerations regarding the manufacturing process of the walls will be discussed, based on the data recorded by the machine by means of the sensors installed on it, as described in Figure 2. The parameter set was tested with three conditions in two cooling time strategies. On the one hand, with the interpass cooling strategy, a cooling time of 180 s is set, and the controlled overlayer strategy is used to wait until 500 °C to start the next welding pass. These cooling times are necessary for the solidification of the pass to take place and when the next one begins, there is no collapse of the wall. With the COS strategy, the cooling time is shorter, for which it is necessary to have the measurement of the surface temperature of the bead by means of the pyrometer.

The following Figure 5 shows the signal registered after the completion of the 12 layers with which the wall is manufactured. In the case of the ICS strategy, the total cooling time rises to 2000 s, consisting of the cooling time (12 weld passes for 180 s) and preparation time for the next pass. In the case of the COS strategy, the time required for the surface to reach 500 °C is less than in the first passes, and increases until it reaches a stationary level. In the case of ICS strategy, heat on the surface of the welding pass decreases due to an initial phase of thermal conduction to the rest of the wall and substrate. Subsequently, heat dissipation occurs due to convection in the area around the wall, so the temperature initially drops rapidly to about 300 °C and then slowly. Then, 180 s of waiting was selected to guarantee the incursion of the convection phase.

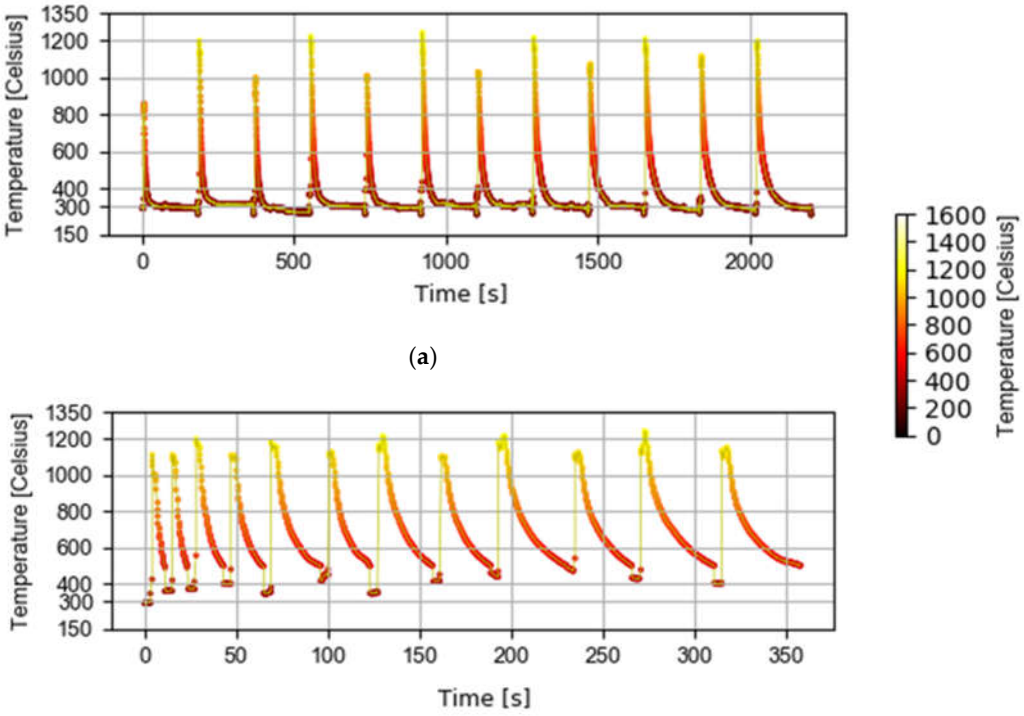

(**a**)

(**b**)

Figure 5. Surface temperature on the interlayer cooling time with strategies (**a**) A_ICS and (**b**) A_COS.

The same strategies were carried out for the set of deposit conditions B and C. Figure 6 shows the evolution of the surface temperature of the welding pass in the cooling times of the 12 layers in the two cooling strategies with the two deposition conditions. In both cases, the cooling temperature in the case of the COS strategy begins at lower maximum temperatures for the first layer, which then increases. When the first layer is made the substrate is cold therefore heat flows from the wall surface by conduction to the substrate. Being the cooling times lower in the first passes in the COS strategy. As a general term, COS strategy is more efficient from the point of view of parts manufacturing times, reducing cooling times by more than 80%. Some novel strategies could be applied to try to take advantage of those waiting times such as manufacturing more than one piece at a time.

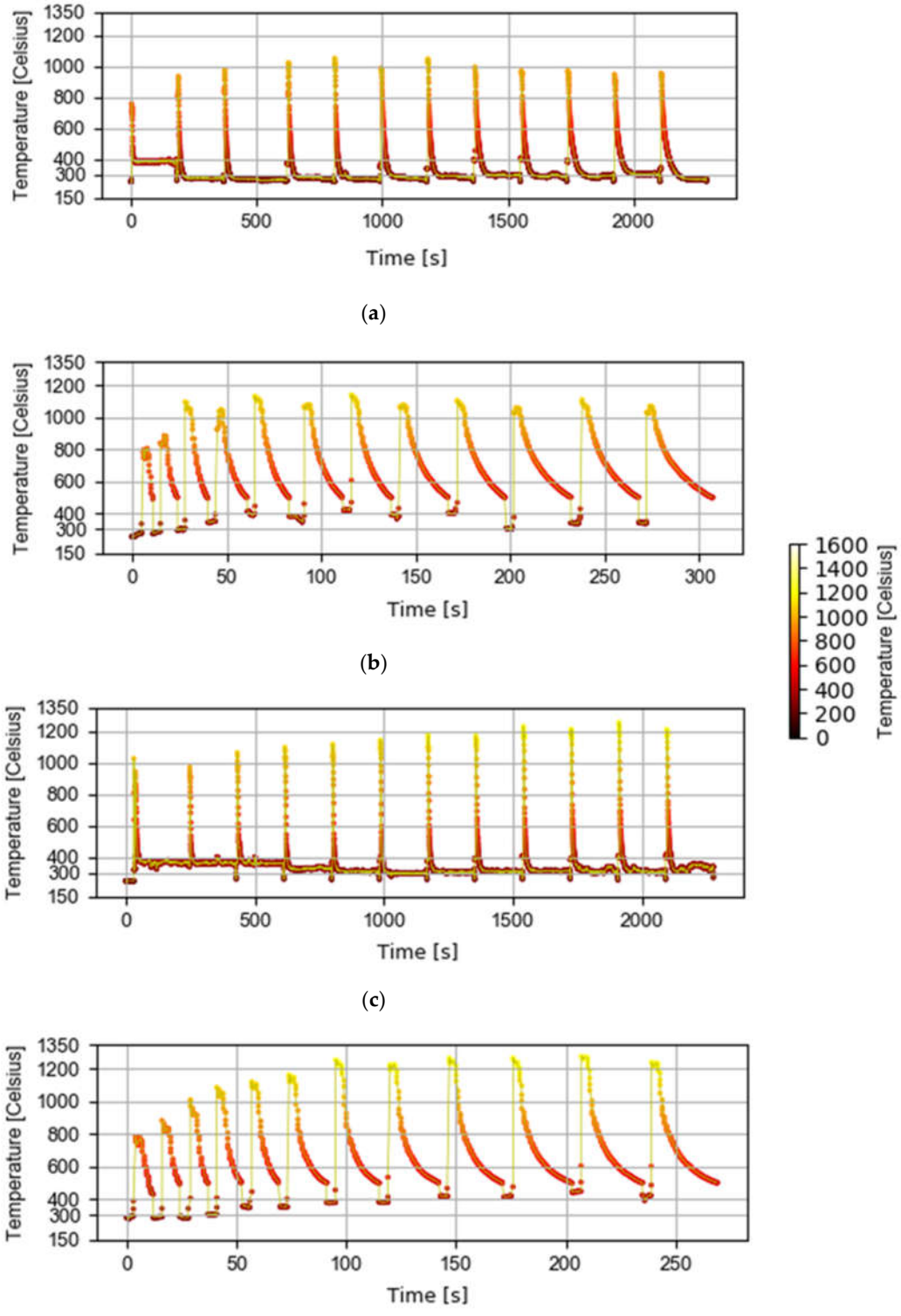

Figure 6. Surface temperature on the interlayer cooling time with strategies (**a**) B_ICS, (**b**) B_COS, (**c**) C_ICS and (**d**) C_COS.

The parameters of the power source were monitored, in Figure 7 the average current and voltage values are shown with their deviation in the 12 passes of the weld passes deposited. On the one hand,

we have a higher wire feed speed with A adding conditions, so the total power (current × voltage) is greater. In the other two sets of conditions (B and C) the same power was maintained for the two wire feed speeds tested. Constant values are observed over the different passes on the three sets of conditions and cooling strategies.

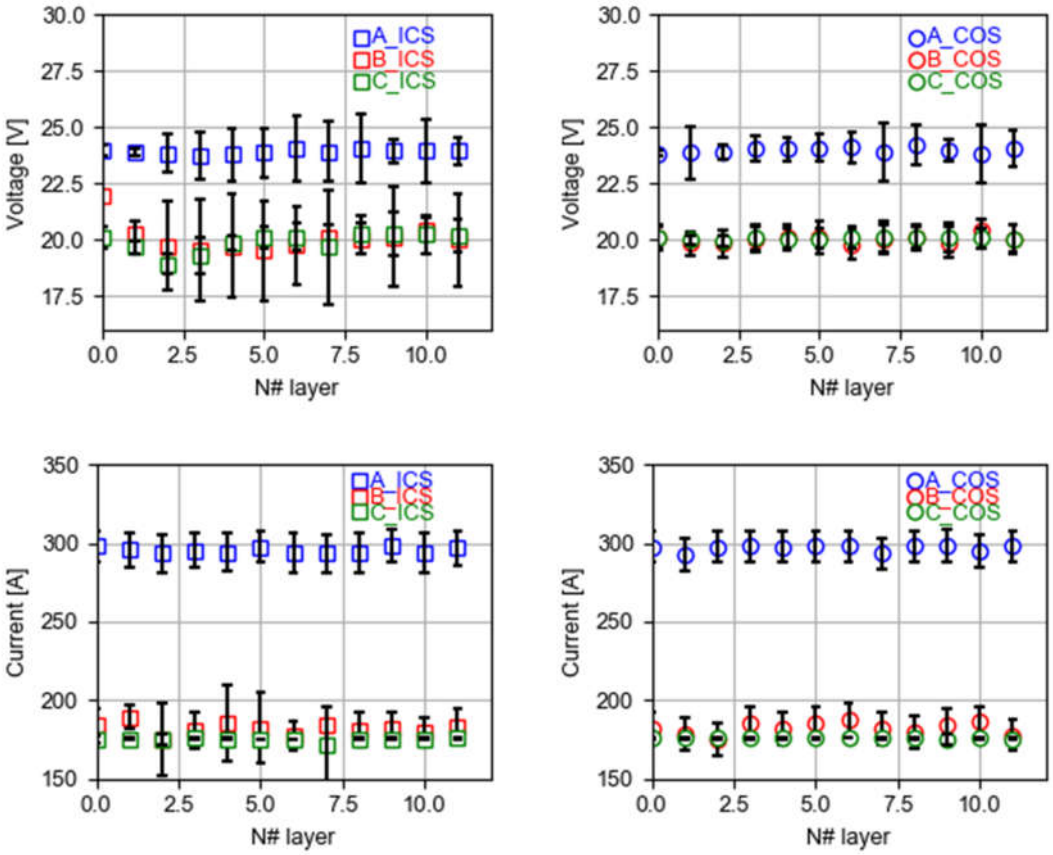

Figure 7. Mean and standard deviation of the current and voltage on the different adding conditions and cooling strategies.

Having the current (I) and voltage (V) measured in a layer we could obtain the total energy per wire feed that Equation (1) would follow. Equation (2) reflects the deposition energy per mm of travel movement.

$$Ed = {I \cdot V}/{TTS} \text{ [J/mm]} \quad (1)$$

$$E_w = {I \cdot V}/{WFS} \text{ [J/mm]} \quad (2)$$

The energy required to melt a metal (Em) is that necessary to raise its temperature to its melting point; therefore, being a function of mass (m), specific heat (c_p) and the difference in temperature from the melting point T_f to room temperature T_0 as shown in Equation (3). The mass is the product of the density ρ, and the wire volume ($\varnothing_w$: wire diameter and L_w: 1 mm).

$$Em = m \cdot c_p \cdot (T_f - T_0) \text{ [J/mm]} \quad (3)$$

where, $m = \rho \cdot \pi \cdot \left(\frac{\varnothing_w}{2}\right)^2$.

The relation of energy that would be necessary to melt the wire and the energy that would go directly to the piece to heat the substrate are defined by MR (Melting Ratio) in Equation (4).

$$MR = {}^{Em}/_{Ew} \text{ [J/J]} \quad (4)$$

The following values were used as constants for the Inconel 718 (density ρ: 8.19 g/cm^3, specific heat cp: 0.435 J/g°C, melting temperature T_f = 1300 °C). Table 3 was constructed to summarize the energy consumption in each set of adding conditions.

Table 3. Process parameters for the manufacture of IN718 WAAM wall.

Test ID	V: Voltage (V)	I: Current (A)	E_w: Wire Energy (J/mm)	E_d: Deposition Energy (J/mm)	E_m: Melting Energy (J/mm)	MR (J/J)
A_ICS-A_COS	24	300	72	1075	5.1	0.07
B_ICS-B_COS	20	180	86,4	939	5.1	0.06
C_ICS-C_COS	20	180	144	939	5.1	0.04

Figure 8 shows the growth per layer according to the deposition condition and cooling strategy. The tests under ICS cooling strategy have grown more than the controlled overlayer strategy. The difference between ICS and COS velues is slight and is since the deposition of material on a hot layer produces less growth in the vertical direction. Growth is related to the relationship between torch speed and wire feed speed (TTS/WFS A: 14.93 mm/mm, B: 10.87 mm/mm and C: 6.5 mm/mm). A_ICS and A_COS adding conditions have the highest ratio, and therefore, the growth per layer is the largest. In addition, as it can be shown in Table 3, heat flows to the substrate relatively less since the heat used to melt down the wire is higher in relation to the total amount of heat that goes into the system allowing to have more grown in each pass. Having a significantly higher bead can cause high-temperature gradients to appear inside it, so it may not always be a correct manufacturing condition.

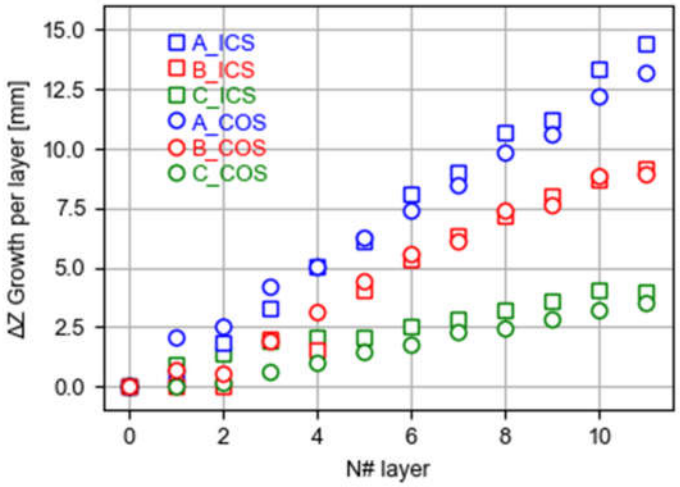

Figure 8. Growth per layer according to the deposition condition and cooling strategy.

3.2. Microstructure Characterization of the Heat-affected Zone (HAZ)

The effect of interpass cooling temperature and different processing parameters on the microstructure of the fusion zone and heat-affected zone (HAZ) is shown in Figure 9. The IN718 WAAM walls fabricated using the plasma arc welding process shows no porosity defect in the cross-sections. It can be found that columnar grains that grow (dendritic structure) epitaxially along the deposition direction are clearly visible in all samples in both ICS and COS. The columnar grains are more coarsen in the controlled overlayer strategy (COS) than in the interpass cooling strategy (ICS),

resulting in the reduction of the contrast, which made it difficult to characterize the interlayer boundaries.

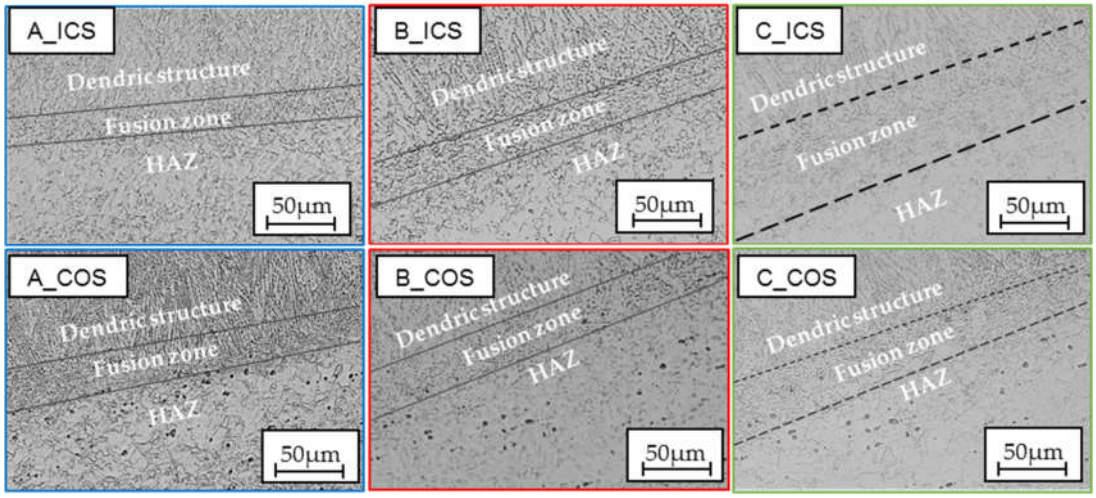

Figure 9. Optical microscopic images microstructure of substrate (base plate) in cross-section view and transition grain structure of the IN718 wall for ICS and COS using both processing parameters.

In addition, the micrograph of the dendritic structure of all samples is shown in Figure 10. All the samples show the fine columnar dendrite structure without secondary dendrites. The main differences between the ICS and COS strategies are the dendritic arm spacing and good continuity of dendritic growth within two adjacent layers. The dendritic arm spacing for the ICS sample is larger than that for the COS samples. Because of this, the formation of the phases is more separated in ICS. Hence, the ICS specimen exhibits a better microstructure than the COS specimen.

The ICS specimen exhibits a better microstructure than the COS specimen. However, the controlled overlayer strategy may cause excessive heat accumulation, resulting in higher molten pool temperature and larger remelting of the substrate or the underlying layers. This causes the poor mechanical properties of the WAAM material. In addition, cracks appeared in the A and C strategies except in B_ICS and B_COS, and it is because the higher heat accumulation in the underlying layers and heat in the molten pool allows the formation of phases in the dendritic arms.

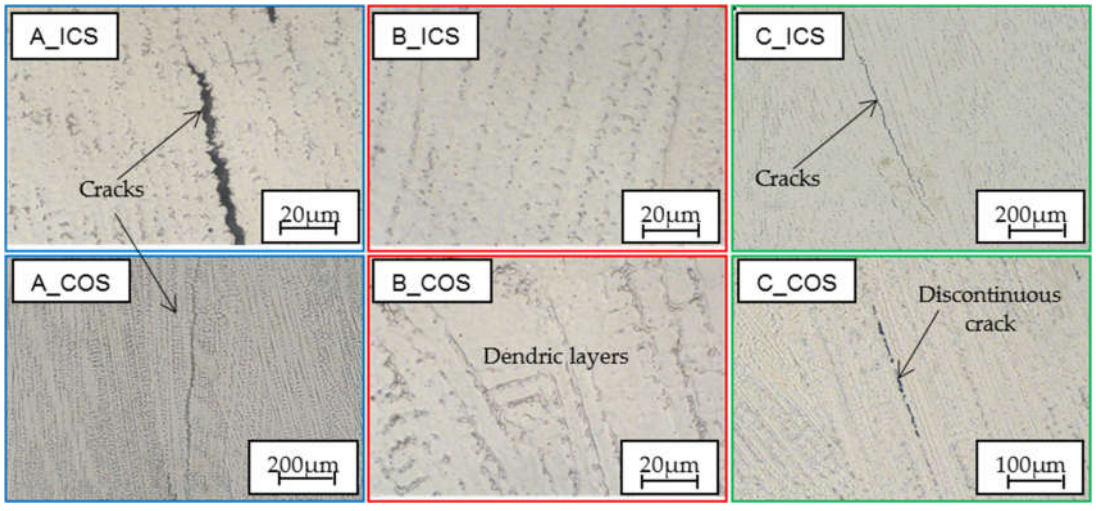

Figure 10. Micrograph of dendritic structure for the ICS and COS samples.

3.3. Apparition of Laves Phase and Hot Cracking Formation

A large number of irregular shape phases and some small blocky particles were precipitated in the interdendritic regions, as shown in Figure 11a. The XRD (X-ray diffraction) analysis is performed to identify the precipitates in WAAM IN718 samples; Figure 11 shows the example sample. The diffractometer used in this study is a Bruker D8 Advanced with Bragg–Brentano configuration with Cu-K_α radiation. From Figure 11b, it shows that the Laves phase (2theta-47.82), (2theta-77.56) with the lattice cell parameter of a = 0.478 mm, c = 0.795 nm, exists in the microstructure. Moreover, because of the low volume fraction of Laves phase and metal carbides (MC) compared with the γ matrix (2theta-52.62, a = 0.358 nm), its diffraction peak is very weak. However, the diffraction peak of carbide is too weak compared to the Laves phase; it is assumed that it is drowning in the basal peak. According to this method, it is suggested that the phase particles in WAAM IN718 consist of Laves phases and carbides.

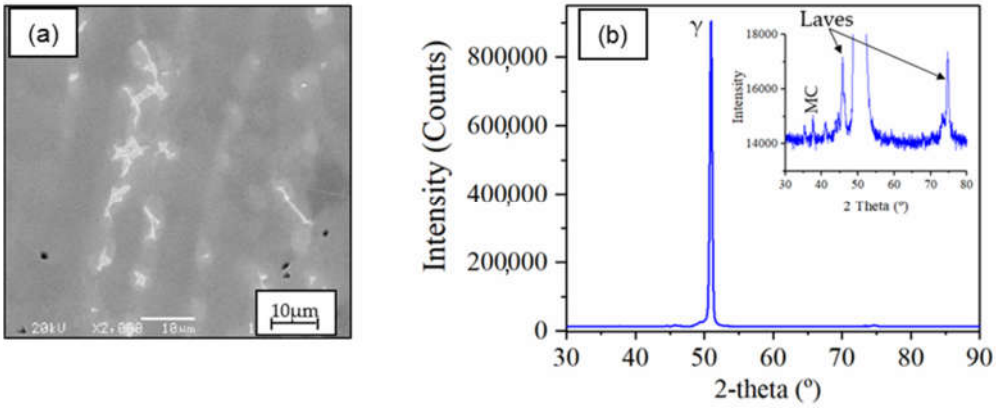

Figure 11. (**a**) the microstructure and corresponding (**b**) XRD pattern of WAAM IN718.

The diffusion and size of the Laves phase in the WAAM microstructures are related to the nature of the dendritic solidification structure. The presence of the Laves phase is evidence of elemental segregation caused by high heat input and slow cooling rate [20] during deposition of the layers. The formation of the Laves phase and MC carbides is due to the segregation of refractory elements Nb and Mo in the nonequilibrium solidification conditions.

The Scanning Electron Microscope (SEM) graphs demonstrate the precipitated phases appearing in the microstructure of the ICS and COS samples, as shown in Figure 12. The samples come from the ICS strategy; the precipitation of the Laves phases appeared for all given samples. In A_ICS and C_ICS samples, the Ti and Nb rich inclusion (or MC) occurred in the alloy matrix and some in the white island. It means that there is large segregation of these element components in those samples compared to the B_ICS sample. This enrichment, deleterious the microstructure failure and possibly crack can appear in the interdendritic region.

While in B_ICS, the inclusions do not appear in the matrix, and the microstructure of B_ICS seems more homogeneous without the appearance of cracks. This is because the thermal gradient during the fabrication of the B_ICS sample is lower compared to the other two strategies (A and C) that lead to faster solidification. As can be seen in Figure 12, in B_ICS, the appearance of the Laves phase (white particle) and carbides are very small in size and sparsely populated compared to the other samples.

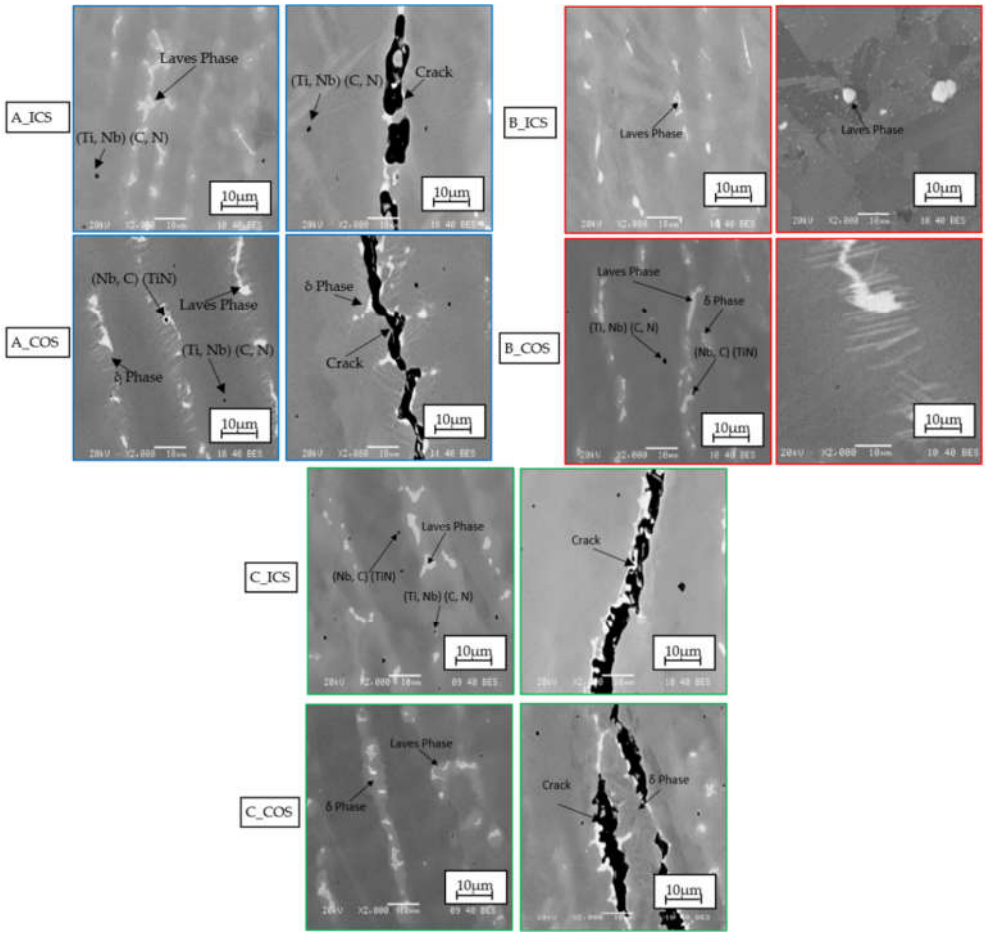

Figure 12. SEM graphs of the precipitated phases observed in the microstructure of the ICS and COS samples**.**

The microstructure observed in the COS samples are different; the main differences between the ICS and COS samples are the composition segregation and distribution characteristics of precipitation phases. It is shown in Figure 12 (A_COS, B_COS and C_COS) that a few needle-like phases are precipitated in the interdendritic regions, including the Laves phase. The needle-like phases are identified as a δ-phase [21] and it is also observed by the XRD analysis. The presence of this δ-phase is more in the A_COS samples than in B_COS and C_COS samples. Hence, the occurrence of the δ-phase entirely depends on the solidification time and processing parameters used for manufacturing. In addition, it is also observed that in the COS samples (A_COS and C_COS), continuous cracks appear near the δ-phase, which is more intensely populated in the inner region than in the ICS sample.

In order to study the phases by their element composition and the composition related to cracks in the interior region, etc., EDS (energy-dispersive X-ray) spectroscopy was performed on each sample. The three types of constituents are selected: coarse white particles (inside a yellow circle), matrix (inside the blue rectangle) and constitute near the crack (green square) as shown in Figure 13. The white particles seem to have particular shapes and appear to be present along with the dendritic structure.

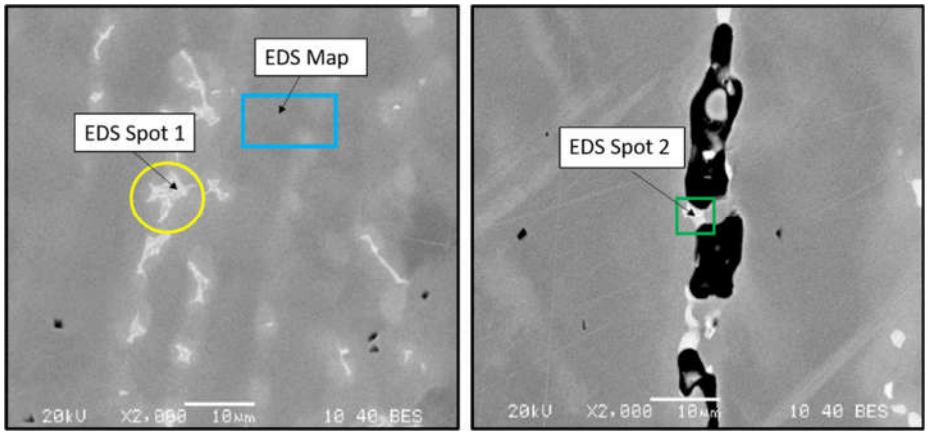

Figure 13. BSE images depicting the matrix, white intermetallic and constitute near the crack in the microstructure.

EDS scans were performed over an area (EDS map), at points (EDS Spot 1) and (EDS Spot 2) to obtain the nominal chemical composition of the WAAM IN718 matrix, the white intermetallic phase (considered to be Laves phase) and composition of elements near hot cracking, respectively. Figures 14 and 15 give the composition of the matrix and white intermetallic phases. This analysis is only a semi-quantitative presentation without more standardization. So, the contents found in this study Figure 14 are consistent with that of general IN718 wire content reported in Table 1.

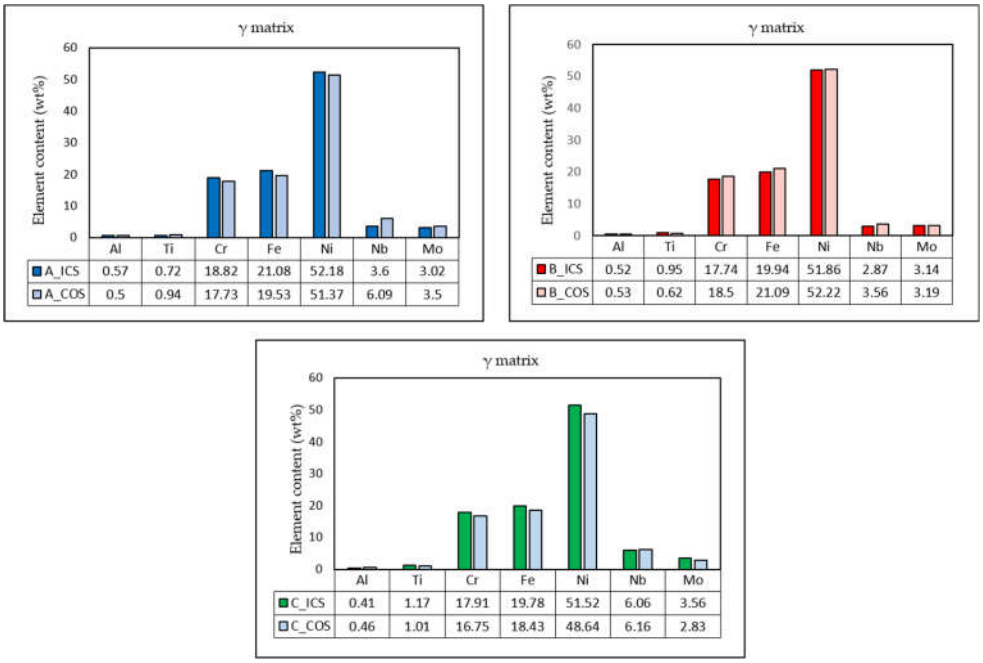

Figure 14. Comparison of γ matrix in the different deposition strategies (EDS map).

From Figure 14, for all the samples, the main elements in the γ-matrix, which are represented by the EDS map, are more abundant in Ni, Cr and Fe, as shown by their peaks and smaller peaks were observed for Nb and Mo. In addition, the composition of the elements for the Laves phase particles is shown in Figure 15, and it is represented by the EDS Spot 1, Laves phase is made up of Cr, Fe, Ni, Nb and Mo elements. The niobium content of the Laves phase of the dendritic core area is higher in the microstructure of COS compared to the ICS. This indicates heavier segregation than the case of the interpass cooling strategy (ICS).

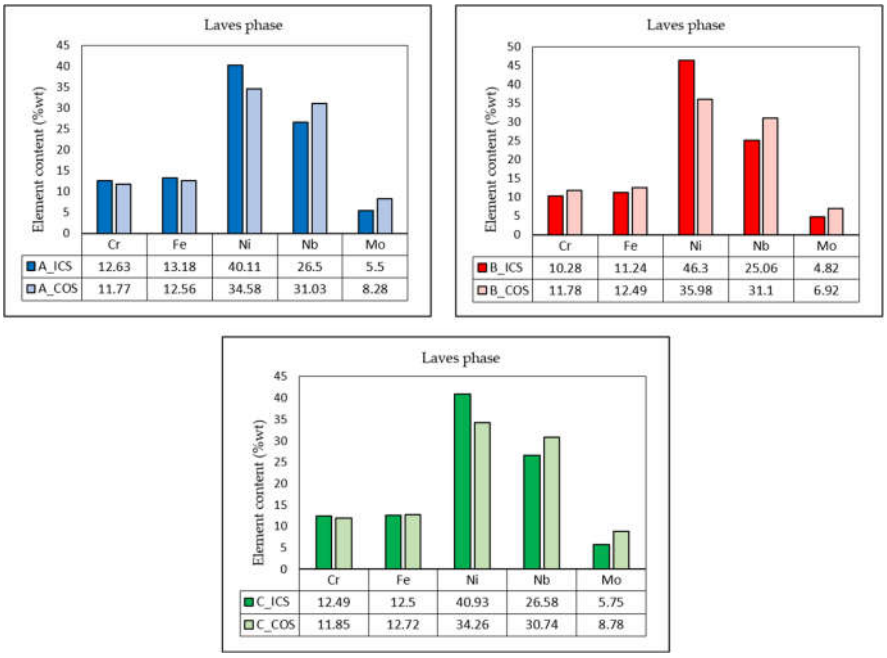

Figure 15. Comparison of Laves phase in the different deposition strategies (EDS Spot 1).

As a result of that, from Figures 14 and 15, the segregation of the enrich elements (Nb and Mo) in the matrix of A and C samples are slightly higher than in the B sample. In addition, the composition of the Laves phases shows a similar kind of behavior for all samples. However, for COS samples, the amount of enrichment was moderately higher than for ICS samples.

In the WAAM process, the solidification of the Inconel 718 alloy begins with the first liquid γ matrix, causing the accumulation of elements Nb, Mo, C and Ti in the interdendritic liquid and grain boundaries. Thus, the Laves phase, MC carbides (including NbC and TiC) and δ phase can be precipitated in these regions. The subsequent liquid eutectic reaction (γ + NbC) then consumes most of the available carbon until another eutectic reaction (γ + Laves) occurs, completing the solidification process [22]. The Laves phase is an unavoidable terminal solidification phase in the Inconel 718 alloy. However, solidification conditions can strongly influence the extent of niobium segregation and the amount of Laves phase [23]. It can be seen from Figure 14 that a high cooling rate causes less segregation of the alloying elements (such as niobium, molybdenum) due to insufficient time for solute redistribution when ICS is used. Laves phase precipitation consumes so many alloying elements, including niobium and molybdenum, in the solidification process of WAAM–PAW that little niobium elements remain for the precipitation of the needle-shaped delta phase. Therefore, the delta phase cannot be formed in the ICS process.

On the contrary, when COS is used, the low cooling rate results in greater segregation of the alloying elements. Then, the solidification process of WAAM–PAW ends with the eutectic reaction (γ + Laves + δ), caused by the accumulation of alloying elements in the residual liquid after the Laves separation phase. This can be seen in Figure 11 that certain needle-shaped delta phases develop along the edges of the Laves particles in COS strategies. In addition, the formation of the δ phase reduces the mechanical properties of the sample and makes the sample more brittle. The formation δ phase can accelerate the propagation of the cracks from the Laves phase particle.

Analyzing the EDS Spot 2 chemical composition of the crack surface gives the statistical result of as 26 wt % Nb, 7.18 wt % Ti, 6.02 wt % Al and 9.94 wt % C. It reveals that the crack surface was fragmented with Nb-, Al-, and Ti-enriched phases, the concentrations of these elements in the A and C samples are higher than those in the B samples. The results suggest that the crack in microstructure is liquation cracking [14]. The enriched alloy elements produce a constitutional liquation in the segregated region due to the high heat and cracks that formed because of the thermal stress. As the

temperature decreased, the alloy element-enriched molten metal solidified at the final stage of solidification, with the precipitate phase generated at the crack surface.

A greater number of longer cracks emerge in samples of the WAAM wall, as shown in Figure 11. Meanwhile, the Laves phase precipitates appear in a greater number around the cracks mostly in the samples coming from A and C. The heat accumulation is much higher in these samples, creating the molten pool in the inner boundaries of dendritic structure. As a result, the cracks can be identified as liquation cracking [14]. The grain boundary liquefies due to the high-temperature process, followed by the molten metal solidifying and the Nb-enriched Laves phase precipitating during the time it cools. If there are more Laves phase precipitates around the cracks, this implies lower melting point molten metal in the dendritic in the final stage of solidification. This is a good time for hot cracks to appear, in the case the liquid segments connect, stretching along the dendritic arm.

4. Conclusions

In this paper, three different addition conditions with similar deposition energies were analyzed (A: 1075 J/mm, B and C: 939 J/mm). The choice of the opposite direction in the alternative layer was used to avoid geometric errors. Two waiting strategies were tested after the layer was made, ICS (interpass cooling strategy) consisting of a fixed waiting time and COS (controlled overlayer strategy) with temperature control on the surface of the weld pass. The following conclusions can be drawn from this work:

- Regarding manufacturing times, the COS strategy, although it involves the installation of a pyrometer, reduces the times by more than 80%.
- Growth per layer is greater in the strategy with higher deposition rates which was to be expected. Regarding the cooling time strategy, the walls made with ICS have slightly higher growth.
- From the microstructural analysis, it shows that the spacing of the dendritic arms for the ICS sample is greater than that of the COS samples. As a consequence, the formation of Laves phases is more discrete in ICS. SEM analysis shows the formation of Laves phases and metallic carbides (inclusion of MC such as Ti and Nb) in the interdendritic region of each sample.
- For ICS samples, the enrichment of Nb and Mo is significantly reduced due to a higher cooling rate. It is observed that the sample from the B_ICS has a homogeneous and crack-free microstructure than the A_ICS and C_ICS samples. However, for the COS samples, the low cooling rate of the layers results in a high-temperature build-up in each layer, allowing greater segregation and the formation of the δ phase (needle-shaped) which aggravates the microstructure and makes the sample more brittle.
- The hot cracks that can be seen in the microstructure of the WAAM walls are liquefaction cracks. However, it shows that samples B_ICS and B_COS do not show cracks in the inner region compared to the other samples from A and C. Therefore, it indicates that the crack formation is fully controlled by the processing parameters (such as B: E_d: 939 J/mm, TTS: 230 mm/min), WFS: 2.5 m/min and DR: 1.39 kg/h) used for this study.

Author Contributions: Conceptualization, F.V.; Data curation, T.B. and F.V.; Investigation, T.A., T.B. and F.V.; Methodology, T.A. and A.S.; Project administration, A.S.; Supervision, A.S. and A.L.; Validation, T.B.; Writing – original draft, T.A., T.B. and F.V.; Writing – review & editing, A.S. and A.L. All authors have read and agreed to the published version of the manuscript.

Funding: The authors acknowledge the Basque Government ELKARTEK 2019 program (KK-2019/00004) and HARIPLUS project, HAZITEK 2019 program (ZL-2019/00352) and to the European commission through EiT Manufacturing programme in DEDALUS project (reference ID 20094).

Conflicts of Interest: The authors declare no conflicts of interest.

References

1. Gloria, A.; Montanari, R.; Richetta, M.; Varone, A. Alloys for aeronautic applications: State of the art and perspectives, *Metals* **2019**, *9*, 662

2. Ford, S.; Despeisse, M. Additive manufacturing and sustainability: an exploratory study of the advantages and challenges. *J. Cleaner Prod.* **2015**, *137*, 1573–1587
3. *Diagnosis and study of opportunities of metallic additive manufacturing on sudoe aerospatial sector.* AFM, Posted October 31, 2017. Available online: http://www.addispace.eu/gestor/recursos/uploads/imagenes/noticias/INFORME/State_of_the_art_MAM-ENGLISH_low.pdf. (accessed on 01/05/2019)
4. Mikolajczyk, T.; Malinowski, T.; Moldovan, L.; Fuwen, H.; Paczkowski, T.; Ciobanu, I. CAD CAM System for Manufacturing Innovative Hybrid Design Using 3D Printing. *Procedia Manuf.* **2019**, *32*, 22–28.doi:10.1016/j.promfg.2019.02.178.
5. Ding, D.; Pan, Z.; Cuiuri, D.; Li, H. Wire-feed additive manufacturing of metal components: technologies, developments and future interests. *Int. J. Adv. Manuf. Technol.* **2015**, *81*. 465-481, doi:10.1007/s00170-015-7077-3.
6. Clark, D.; Bache, M.R.; Whittaker, M.T. Shaped metal deposition of a nickel alloy for aero engine applications. *J. Mater. Process. Technol.* **2008**, *203*, 439–448.
7. Clark, D.; Bache, M.R.; Whittaker, M.T. Microstructural characterization of a polycrystalline nickel-based superalloy processed via tungsten-intert-gas-shaped metal deposition. *Metall. Mater. Trans. B* **2010**, *41*, 1346–1353.
8. Baufeld, B. Mechanical properties of INCONEL 718 parts manufactured by shaped metal deposition (SMD). *J. Mater. Eng. Perform.* **2012**, *21*, 1416–1421.
9. Knezović, N.; Topić, A. *Wire and Arc Additive Manufacturing (WAAM)–A New Advance in Manufacturing, in Lecture Notes in Networks and Systems*; Springer Nature Switzerland AG; **2019**; Volume 42, pp. 65-71.
10. Manikandan, S.G.; Sivakumar, D.; Kamaraj, M.; Rao, K.P. Laves phase control in Inconel 718 weldments. *Mater. Sci. Forum* **2012**, *710*, 614–619.
11. Antonsson, T.; Fredriksson, H. The effect of cooling rate on the solidification of INCONEL 718. *Metall. Mater. Trans. B* **2005**, *36*, 85–96. doi:10.1007/s11663-005-0009-0.
12. Ling, L.; Han,Y.; Zhou, W.; Gao, H.; Shu, D.; Wang, J.; Kang, M.; Sun, B. Study of Microsegregation and Laves Phase in INCONEL718 Superalloy Regarding Cooling Rate During Solidification. *Metall. Mater. Trans. A* **2015**, *46*, 354–361.
13. Seow, C.E.; Coules, H.E.; Wu, G.; Khan, R.H.; Xu, X.; Williams, S. Wire + Arc Additively Manufactured Inconel 718: Effect of post-deposition heat treatments on microstructure and tensile properties. *Mater. Des.* **2019**, *183*, 108157.
14. Ye, X.; Hua, X.; Wang, M.; Lou, S. Controlling hot cracking in Ni-based Inconel-718 superalloy cast sheets during tungsten inert gas welding. *J. Mater. Process. Technol.* **2015**, *222*, 381–390.
15. Deng, D. Additively Manufactured Inconel 718: Microstructures and Mechanical Properties. Licentiate Thesis, Linköpings Universitet. Institutionen för ekonomisk och industriell utveckling. Linköping, Sweeden, January 2018.
16. Xu, F.; Lv, Y.; Liu, Y.; Shu, F.; He, P.; Xu, B. Microstructural Evolution and Mechanical Properties of Inconel 625 Alloy during Pulsed Plasma Arc Deposition Process. *J. Mater. Sci. Technol.* **2013**, *29*, 480–488.
17. Yang, W.; Xi, C.; Chuan, S. Microstructure and mechanical properties of Inconel 625 fabricated by wire-arc additive manufacturing. *Surf. Coat. Technol.* **2019**, *374*, 116–123.
18. Xu, X.; Ganguly, S.; Ding, J.; Seow, C.E. Williams, S. Enhancing mechanical properties of wire + arc additively manufactured INCONEL 718 superalloy through in-process thermomechanical processing *Mater. Des.* **2018**, *160*, 1042–1051.
19. Zhang, J.; Zhang, X.; Wang, X.; Ding, J.;Traoré, Y.; Paddea, S.; Williams, S. Crack path selection at the interface of wrought and wire + arc additive manufactured Ti-6Al-4V. *Mater. Des.* **2016**, *104*, 365–375.
20. Xu, X.; Ding, J.; Ganguly, S.; Williams, S. Investigation of process factors affecting mechanical properties of INCONEL 718 superalloy in wire + arc additive manufacture process. *J. Mater. Process. Technol.* **2019**, *265*, 201–209.
21. Mahadevan, S.; Nalawade, S.; Singh,J.B.; Verma, A.; Paul, B.; Ramaswamy, K. Evolution of δ Phase Microstructure in Alloy 718, In Proceedings of the 7th International Symposium on Superalloy 718 and Derivatives, Pittsburgh, PA, USA, 10 - 13 October **2010**.

22. Ram, G.D.J.; Reddy, A.V.; Rao, K.P. Improvement in stress rupture properties of Inconel 718 gas tungsten arc welds using current pulsing. *J. Mater. Sci.* **2005**, *40*, 1497–500.
23. Madhusudhan, G.; C. Srinivasa, C.; Srinivas, K. Improvement of mechanical properties of Inconel 718 electron beam welds-influence of welding techniques and post weld heat treatment, *Int. J. Adv. Manuf. Technol.* **2009**, *43*, 671–680.